No-Flow Impedance Models for Open-Variable-Depth Chambers

Jordan Kreitzman

NASA Langley Research Center, Hampton, VA, 23681-2199, USA

Abstract

A surface impedance modeling approach for open-variable-depth chambers in a no-flow environment is described that takes into account the self and mutual radiation impedance of each chamber. This approach is compared in accuracy and efficiency to other established methods, using experimental data from a variety of samples tested in a no-flow, normal-incidence impedance tube at relatively low sound pressure levels (<100 dB). It is found that the new approach described in this study is similar in accuracy to finite-element methods while operating at orders-of-magnitude lower computational time. A low-frequency approximation to the proposed method further improves model efficiency while maintaining accuracy, at least for the samples and test conditions considered in this study. Finally, a prediction study is shown that assesses the need for modeling radiation impedance of open-variable-depth, narrow-width chambers, illustrating that radiation effects should also be modeled for these samples, at least for higher frequencies (3000–6000 Hz). This prediction technique lays the foundation for future models designed to capture impedance for realistic variable-depth liners in grazing-flow environments, such as perforated facesheet liners in an engine nacelle.

Keywords: acoustic liner, variable depth, open chamber, radiation impedance, normal incidence, prediction model, transmission line

1. Introduction

Future subsonic transport aircraft designs have been trending toward the use of higher-bypass-ratio engines and shorter nacelles for increased fuel efficiency. This has increased the contribution of fan noise to the overall engine noise, which is the dominant source of aircraft noise for most flight conditions [1]. Additionally, improvements in engine fan designs have lowered the tonal noise signature, increasing importance of the fan broadband noise [2, 3]. Improving acoustic liners embedded within the engine nacelle walls to more effectively absorb fan noise is therefore a critical part of meeting current and future stringent demands of aircraft noise regulations. This allows commercial aircraft fleets to continue to grow without significantly impacting the surrounding public near airports.

However, these engine trends also negatively impact acoustic liner effectiveness. This is due to reduced surface area for treatment and increased liner volume required to appropriately mitigate

Email address: jordan.r.kreitzman@nasa.gov (Jordan Kreitzman)

the lower-frequency fan noise signature. Identifying previously untreated areas within the nacelle for possible liner implementation is a critical aspect of combating this issue. More comprehensive surface treatment is further complemented by liner designs that absorb a wider range of frequencies and more effectively target optimized design points across multiple flight conditions.

An acoustic liner is typically composed of a perforated facesheet over constant-depth honeycomb chambers with a rigid backing, much like what is shown in Figure 1. The acoustic characteristics of a liner are defined by its surface impedance (ζ), which is the ratio of acoustic pressure (p) to acoustic particle velocity (u) normal to the liner surface. This ratio is shown mathematically as

$$\zeta = \frac{p}{\rho c u} = \theta + \mathrm{i}\chi, \tag{1}$$

where terms are normalized by the characteristic impedance of air, ρc, and impedance is defined in the $\mathrm{e}^{+\mathrm{i}\omega t}$ convention, where i is the imaginary number ($\sqrt{-1}$), ω is angular frequency, and t is time. Note that for the remainder of the article, if i is a subscript, or denoted as the i^{th} of something, it is referring to an index for an array of values. Otherwise, i represents the imaginary number. The impedance contains resistance (θ) and reactance (χ) components, with contributions from the facesheet and chambers.

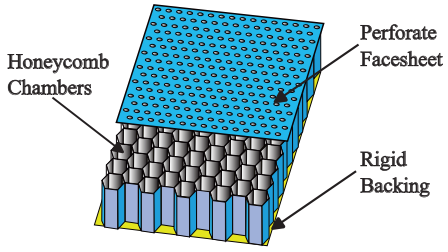

Figure 1: Example of a typical single-degree-of-freedom acoustic liner.

It is critical to improve impedance prediction quality so as to better distinguish between designs, thereby enabling better technological decisions. Older generations of aircraft required liners that could target specific fan tones, and this required prediction models to be accurate at a narrow frequency range. Modern acoustic liner designs need to attenuate a broad range of frequencies, and therefore prediction schemes must also be accurate for a wider range of frequencies [4]. In addition, it is common to design an acoustic liner for a complex environment (e.g., commercial aircraft engine nacelle in flight) but verify its acoustic characteristics in a simple normal-incidence impedance tube. More complex impedance tubes exist (such as grazing flow impedance tubes [5]) that help bridge the gap in environmental complexity, but are not always used in design due to their scarcity and the intricacy involved in data acquisition and processing. Therefore, it is imperative to account for impedance differences between the simple impedance tube and complex environment.

2. Background

One possible acoustic liner design for increased absorption bandwidth is the use of variable-depth chambers, where the acoustic liner is tuned to multiple frequencies depending on individual chamber depth. Figure 2 shows the difference between a constant- and variable-depth chamber array. Research on variable-depth liners has been conducted for some time, particularly once the importance of mitigating fan broadband noise increased [6]. These designs have become more viable over time with the introduction of additive manufacturing [7, 8] but have also been implemented using standard materials and manufacturing practices [9]. Since the impedance spectra of these designs vary spatially, it is necessary to compute effective impedance spectra for larger surface regions rather than just individual chambers. Work has been done to assess the spatial extent at which this effective impedance assumption is valid in grazing acoustic incidence and flow [10]. Research has also been performed to identify variable-depth liner configurations with reduced nacelle drag [11, 12], as well as increased absorption bandwidth utilizing bent, variable-depth chambers with embedded septa [13] as well as without [14]. More recently, variable-depth concepts have also been assessed for potential application on rotorcraft for ducted proprotor noise [15, 16]. These concepts have also been implemented into more complex systems, such as perforated walls between the variable-depth chambers [17] or even variable-depth tubes that extend from the perforated facesheet [18].

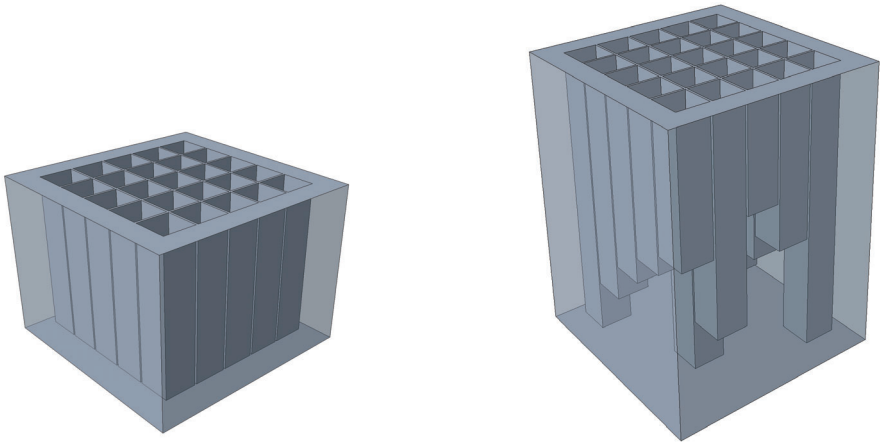

(a) (b)

Figure 2: Examples for (a) constant- and (b) variable-depth chamber layouts.

Typically, surface impedance of an open chamber array (i.e., no perforated facesheet or mesh on top) is predicted with great accuracy if every chamber is at the same depth. However, when a variable-depth chamber array is introduced, prediction errors typically increase. This is due to the enhancement of radiation impedance caused by chambers of different depths radiating out of phase with one another. The radiation impedance of each chamber is due to the radiated pressure

field acting on its surface (interface between chamber and environment) due to itself radiating (self) and other chambers radiating (mutual) into the aeroacoustic environment, divided by its surface particle velocity. These effects are modified by the environment in which the chambers radiate (e.g., semi-infinite vs. duct, no flow vs. grazing flow).

For this particular study, the focus is on chambers radiating into a normal-incidence impedance tube with no grazing flow present. As mentioned earlier, while this is the simplest case, acoustic liner designs often first get tested in these environments, and it is important to predict and identify differences between this testing environment and more complex implementations. Approaches for predicting the mean flow effect on liner radiation impedance often use no-flow models with empirical adjustments [19, 20]. This typically involves testing samples at various flow speeds in a grazing flow impedance tube, scaling down the predicted no-flow radiation impedance to match experiment. Usually the Mach number is used in some form as the scaling parameter. Hence, models for no flow are foundational and often the basis for models with flow. For the frequencies and chamber widths associated with this study, radiation resistance is neglected, as it scales with d_E^2 and not d_E like reactance, where d_E is the effective diameter of the chamber opening. The radiation impedance (ζ_R) is therefore assumed purely reactive and, for a single chamber, modeled as

$$\zeta_R = \mathrm{i}k\delta, \tag{2}$$

where k is the free-space wavenumber, and δ is the mass-end correction term, which can be modeled with or without frequency dependence. The decision to include frequency dependence is typically reliant on the aeroacoustic environment, frequencies of interest, and required accuracy.

Previous work has attempted to properly model the impedance of variable-depth liners. Parrott & Jones [6] utilized a transmission-line model to compute the surface impedance of each chamber separately, and then applied a summation of admittances to calculate the effective surface impedance of the entire liner. While this approach can work well, it does not take into account radiation effects due to out-of-phase radiators caused by chambers of different depths. Radiation impedance variation due to varying depths has greater influence on effective surface impedance when radiators are larger in size, e.g., standard size open chambers ($\geq 0.25''$). Schiller & Jones [21] later attempted to account for radiation impedance by assuming that all chambers radiate in the absence of mutual radiation with other chambers, thereby only accounting for self radiation and modifications due to impedance tube walls. This significantly improved predictions but still lacked sufficient accuracy due to the underlying assumptions. Mutual radiation must be accounted for in the overall prediction process if high accuracy is required.

Early work on the development of the mass-end correction term is traced back to Rayleigh [22], where an end-correction term is defined for a single massless piston in isolation radiating into a semi-infinite environment. This is defined as

$$\delta = \frac{4}{3\pi} d_E. \tag{3}$$

A radiating chamber or perforated facesheet hole is approximated by these massless piston assumptions. This term is still widely used today, but if the piston is radiating into a tube or surrounded by other pistons, it is not an adequate formulation. Fok [23] and Nesterov [24] performed theoretical and experimental studies, respectively, to generate modification functions to Rayleigh's end-correction term to account for a piston radiating into an infinitely-long tube of finite cross section. Later, Ingard [25] performed a detailed study of the radiation impedance of

variously-shaped massless pistons radiating into tubes of different cross-sectional shapes. This included self radiation impedance of pistons at different locations within the cross section of the tube, as well as mutual radiation impedance between two pistons radiating in phase with one another. This work derived the well-known approximate end correction for a single radiating piston located at the center of a tube, given as

$$\delta = \frac{4}{3\pi} d_E (1 - 1.25\sqrt{\phi}), \tag{4}$$

where ϕ is the open area ratio of the piston relative to the cross section of the tube. Due to source-imaging effects from walls [26], this approximation is often used to model radiation impedance of a uniform array of pistons, much like the functions derived from Fok [23] and Nesterov [24]. Ih [27] later expanded Ingard's work, computing self and mutual end corrections of various piston shapes and tubes.

Ingard [25] and Ih [27] focused on development of mutual radiation impedance between two pistons radiating in phase with one another, but Pritchard [28] extended this idea to an arbitrary array of pistons. The total radiation impedance of a piston is the radiated acoustic pressure it creates acting on itself combined with the acoustic pressure acting on it due to every other piston, divided by its surface particle velocity. In other words, one can sum up these individual radiation impedance terms (self and mutual with every other piston) and weight each term by the complex particle velocity ratio between two given pistons, i.e.,

$$\zeta_{R,i} = \sum_{j=1}^{N_C} \zeta_{R,ij} \frac{u_j}{u_i}, \tag{5}$$

where u_i and u_j are surface particle velocities of the i^{th} and j^{th} chambers, respectively, N_C is the number of chambers in the array, $\zeta_{R,ij}$ is the mutual radiation impedance caused by the j^{th} chamber on the i^{th} chamber, and $\zeta_{R,i}$ is the total radiation impedance of the i^{th} chamber. Note that self radiation impedance is included when $j = i$. It is assumed there is a uniform particle velocity distribution at the surface of each chamber. If the pistons are radiating in phase and of uniform intensity with one another, e.g., a constant-depth array of chambers, then this weighting factor is always one. However, if they are radiating out of phase, as is the case with variable-depth chambers, then this weighting term becomes important. While the analysis of Pritchard [28] showed that this particle velocity ratio is present in the computation, the author, like others described previously, focused solely on in-phase radiators and assumed this ratio to be one. Suzuki [29] assessed the mutual radiation impedance of two out-of-phase radiators, noting sizable differences in the performance of each radiator compared to when they radiate in phase.

Some recent work has utilized mass-end correction formulations outlined in Ih [27] and Pritchard [28] to account for differences in radiation impedance due to perforated facesheet hole position [30] and chamber layout [31]. However, in these studies, everything was assumed to radiate in phase with one another, and when out-of-phase radiators existed, assumptions were made to ignore mutual radiation impedance between out-of-phase radiators. This is not a sufficient strategy for open-variable-depth chambers.

The intent of the current study is to document the methodology and results of a new approach for predicting the impedance of open-variable-depth chambers in the absence of grazing flow. This method relies on end-correction formulations provided by Ih [27]. Prediction results are directly compared to experimental data taken from a normal-incidence impedance tube for a variety of open-variable-depth chamber designs. Although the focus is on the normal-incidence

tube, source-imaging effects [26] and careful placement of chambers allow the method to be used for other no-flow environments, such as grazing-incidence tubes or larger area treatment zones. These samples are excited experimentally by relatively low sound pressure level (SPL) tones in order to avoid any nonlinear behavior. However, it is expected for open chambers that the effect of higher SPL excitation on impedance is minimal, due to a lack of significant vortical structures emanating from the chambers. This is in contrast to liners with perforated facesheets, where losses due to turbulent structures from high SPL excitation are much greater. Other established methods for predicting the impedance of variable-depth liners are used to provide additional results for comparison to the new model. Variable-depth chambers without an associated facesheet are the selected samples for this study for a variety of reasons. The radiation effects are much stronger due to larger pistons (chambers instead of holes) radiating into the tube. This allows for a better understanding of the efficacy of each impedance model. It is also often necessary to test the acoustic liner without a facesheet to verify characteristics of the chambers alone.

The surface impedance of chambers without radiation impedance inclusion is also highly predictable, thereby eliminating any uncertainties in the modeling accuracy of the chamber transmission line, providing focus on the accuracy of radiation impedance modeling. Facesheet hole transfer impedance, on the other hand, is much harder to predict accurately (due to uncertainties in geometry, discharge coefficients, etc.), adding additional uncertainty when trying to verify a radiation impedance model. Verification of the model using open chambers lends directly to application with a facesheet though, as the same general process can be applied since facesheet holes are also radiators, albeit smaller ones. Depending on hole position and variable-geometry perforation paths, impact from out-of-phase radiation could still potentially be significant [30, 32], although these effects are typically reduced when grazing flow is present. Accurate modeling of open-variable-depth chambers could also support industries outside of aerospace, such as HVAC and automotive industries, where grazing flows are slower and reactive treatments are desired, effectively redirecting the noise source rather than dissipating it.

The content of the remaining sections of this article is as follows. Section 3 shows a description of the test rig and samples used to validate the impedance models. Section 4 describes impedance prediction formulations for three models. Models 1 and 2 are previous methods used to compute impedance of variable-depth acoustic liners (taken from Parrott & Jones [6] and Schiller & Jones [21], respectively), while Model 3 is the new approach. Model 3 contains both an "a" and "b" variant, associated with low-frequency-approximation and full-formulation approaches, respectively. Next, comparisons of prediction and experimental results are shown in Section 5, followed by a more detailed discussion of prediction errors in Section 6, using an L_2 norm comparison to guide analysis. This includes a brief comparison to prediction errors taken from a finite-element study. Then, a discussion of computational times for Models 1–3 is presented in Section 7. A brief computational study demonstrating the effect of radiation impedance on narrow-width, variable-depth chambers is then shown in Section 8. Finally, a summary of results and next steps is outlined in Section 9.

3. Test Rig and Samples

The Normal Incidence Tube (NIT) at NASA Langley Research Center is a $2'' \times 2''$ waveguide approximately $36''$ long, a solid rendering for which is shown in Figure 3. It uses six BMS Speaker 4599ND $2''$ compression acoustic drivers to generate a sound field that impinges on the acoustic liner surface. There are three flush, wall-mounted microphones associated with the rig. One is a reference microphone $0.25''$ away from the sample surface that is used to provide

feedback in setting the appropriate total (incident plus reflected) SPL for the test. Two other microphones, located 2.50″ and 3.75″ from the liner surface, are mounted in a rotating plug so that their positions can be interchanged [5]. Typically, these two microphones would need to be carefully calibrated to accurately perform the two-microphone method for impedance eduction. However, the position switch of the microphones allows for two measurements to be taken, and the average transfer function is used, effectively eliminating calibration issues [33, 34].

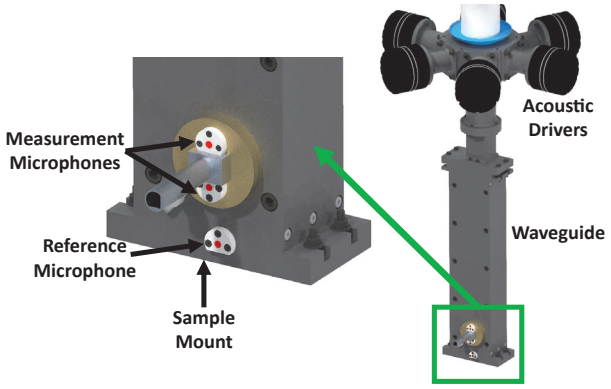

Figure 3: Normal Incidence Tube (NIT) test rig.

The NIT allows for four different source types: stepped-sine, swept-sine, broadband, and multitone at frequencies of 400–3000 Hz [5, 35]. The highest frequency tested in the NIT is kept low enough so that only plane waves propagate within the waveguide. For this particular test, the swept-sine source is used at a total SPL of ~95 dB to avoid any nonlinear behavior. Note that the results include two samples pulled from previous publications that are excited at 120 dB [12, 15]. This is still sufficiently low in amplitude for nonlinear behavior to be minimal. For computing impedance, the two-microphone method is used [33, 34], effectively computing the reflection coefficient directly from the transfer function of the two measurement microphones. With regards to uncertainty, 95% confidence intervals on NIT normalized impedance spectra should be less than 0.02 for samples considered in this study [36].

In order to build an experimental database with a wide range of liner impedances, several variable-depth samples are designed and additively manufactured. Each sample is 3D-printed via Stereolithography, where tolerances of the sample dimensions are generally around ±0.005″. Great care is taken to account for additional effects that can alter tolerances, such as resin bleed from the laser. These samples vary chamber effective diameter and depth as well as the number of unique depths. The chamber depths are selected to distribute resonances of each chamber within the frequency range of 800–3000 Hz. This is done assuming a single chamber (closed on one side, open on the other) resonates when its depth is a quarter of the tonal wavelength. The spacing between chambers is also varied. Additionally, placement of each chamber depth within the array is altered to assess if models successfully capture impedance changes associated with placement differences.

The geometry of each sample is shown in Table 1. Figure 4 shows chamber depth placement for each sample. The numbers on the chambers in Figure 4 represent the distribution of chamber

depths, ordered the same as shown in Table 1, where the depths are written in descending order. Most of the samples have chamber depths that are geometrically in "descending" order, meaning chamber depths go from largest to smallest, starting from the bottom left of the sample and ending at the upper right. An effort is taken for most of the samples to avoid chambers of the same depth next to each other, even diagonally, although it is unavoidable for Sample 2. This is not the case for Samples 10 and 11, which are samples originally made for past publications [12, 15]. These were added later in the process to add further validation for the models, as they have different chamber effective diameters and partition thicknesses. Sample 6, called "similars grouped" in Table 1, has chambers of similar depths placed next to one another. In contrast, Sample 9, denoted as "unlikes grouped" in Table 1, means very different chamber depths are placed next to one another.

Table 1: Sample geometries for wide-chamber liner samples.

Sample Name	Chamber Layout	Chamber Side Length	Partition Thickness	Chamber Depths
1	–	0.375″	0.025″	(1) 1.787″
2	Descending	0.375″	0.025″	(1) 2.215″ (2) 1.498″
3	Descending	0.375″	0.025″	(1) 2.911″ (2) 2.215″ (3) 1.787″ (4) 1.498″ (5) 1.289″
4	Descending	0.275″	0.125″	(1) 2.911″ (2) 2.215″ (3) 1.787″ (4) 1.498″ (5) 1.289″
5	Descending	0.375″	0.025″	(1) 3.251″ (2) 2.635″ (3) 2.215″ (4) 1.910″ (5) 1.679″ (6) 1.498″ (7) 1.352″ (8) 1.232″
6	Similars Grouped	0.375″	0.025″	(1) 3.251″ (2) 2.635″ (3) 2.215″ (4) 1.910″ (5) 1.679″ (6) 1.498″ (7) 1.352″ (8) 1.232″
7	Descending	0.475″	0.025″	(1) 3.251″ (2) 2.635″ (3) 2.215″ (4) 1.910″ (5) 1.679″ (6) 1.498″ (7) 1.352″ (8) 1.232″
8	Descending	0.375″	0.025″	(1) 3.503″ (2) 2.983″ (3) 2.597″ (4) 2.299″ (5) 2.063″ (6) 1.870″ (7) 1.711″ (8) 1.577″ (9) 1.462″ (10) 1.362″ (11) 1.276″ (12) 1.200″
9	Unlikes Grouped	0.375″	0.025″	(1) 3.503″ (2) 2.983″ (3) 2.597″ (4) 2.299″ (5) 2.063″ (6) 1.870″ (7) 1.711″ (8) 1.577″ (9) 1.462″ (10) 1.362″ (11) 1.276″ (12) 1.200″
10	Descending	0.300″	0.100″	(1) 3.751″ (2) 2.701″ (3) 2.110″ (4) 1.731″ (5) 1.350″
11	Descending	0.400″	0.100″	(1) 3.376″ (2) 2.338″ (3) 1.788″ (4) 1.447″

4. Impedance Prediction Theory

The theory behind three impedance prediction models is described below, noting that the new approach is denoted as Model 3. Since open chambers are modeled, it is assumed that nonlinear

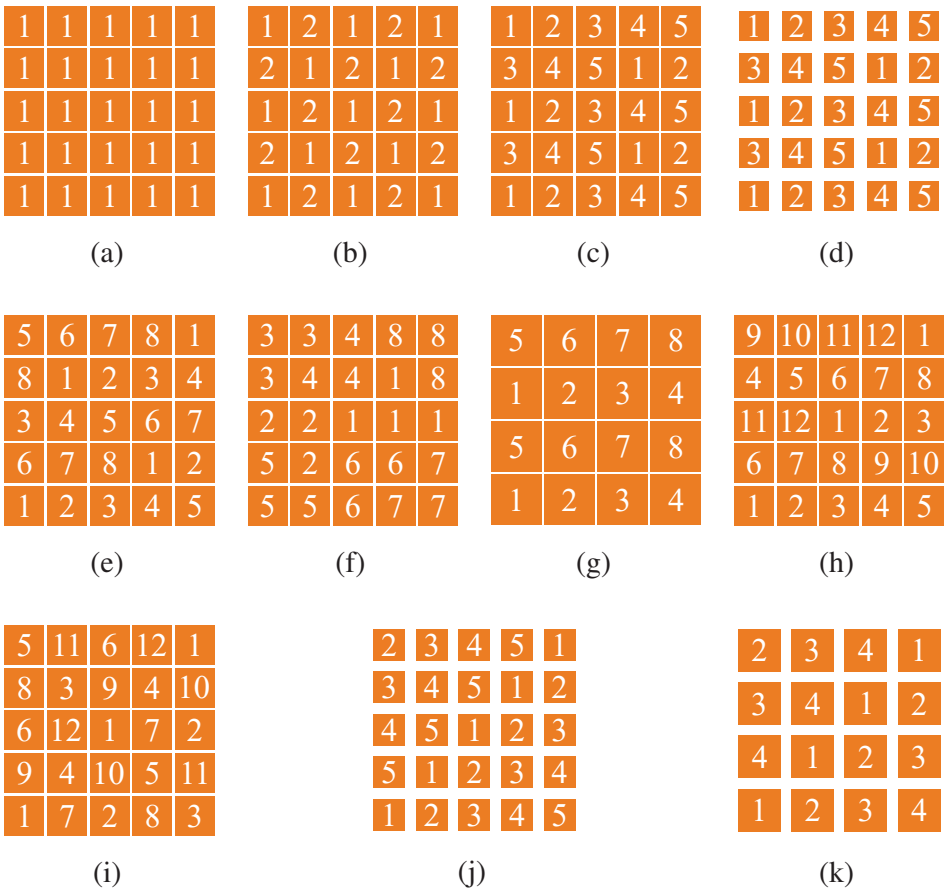

Figure 4: Chamber depth layouts for (a) Sample 1, (b) Sample 2, (c) Sample 3, (d) Sample 4, (e) Sample 5, (f) Sample 6, (g) Sample 7, (h) Sample 8, (i) Sample 9, (j) Sample 10, and (k) Sample 11.

effects do not impact the impedance. All predicted and experimentally educed impedances shown in this report adhere to the $e^{+i\omega t}$ convention. Figure 5 shows the transmission line from backplate to surface of the i^{th} chamber for Models 1–3, where position 0 is the backplate, position 1 is just below the surface, position S is just above the surface, and h_i is the chamber depth. More detail on this is shown in the next section. All models are written into simple Fortran programs for direct comparison, utilizing the LAPACK [37] library when necessary. Finally, for every model, it is assumed that all chambers in a given sample array have the same cross section.

4.1. Model 1: no radiation impedance included

The simplest approach to modeling variable-depth acoustic liner impedance is to ignore the radiation effects ($p_{1,i} = p_{S,i}$, $u_{1,i} = u_{S,i}$ in Figure 5). Each chamber's surface impedance is computed separately and combined at the end via a summation of admittances, including the effect

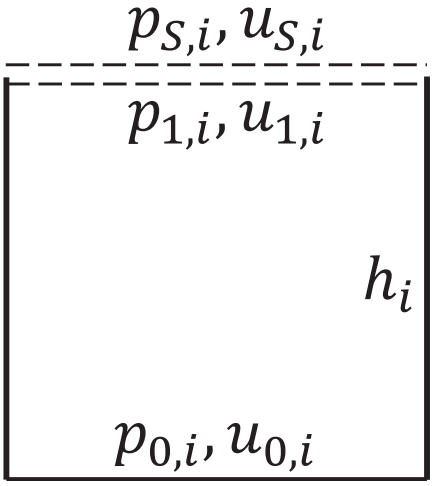

Figure 5: Transmission line from backplate to surface of i^{th} chamber.

of partition thickness between chambers. One can use the transmission-line approach outlined in Parrott & Jones [6] to compute the surface impedance of each chamber, where the complex acoustic pressures and velocities are computed by stepping through the acoustic liner, from backplate to chamber surface. This approach is more accurate when radiators are smaller in diameter, and therefore radiation effects are smaller. It is assumed that the backplate is impervious, and the backplate boundary condition is described as

$$\begin{pmatrix} p_{0,i} \\ u_{0,i} \end{pmatrix} = \begin{pmatrix} 1 + 0\mathrm{i} \\ 0 + 0\mathrm{i} \end{pmatrix}, \tag{6}$$

where $p_{0,i}$ and $u_{0,i}$ are the acoustic pressure and particle velocity, respectively, at the backplate of the i^{th} chamber. These values are normalized by the density of air multiplied by the speed of sound squared, ρc^2, and speed of sound, c, respectively. Transmission coefficients are used to compute pressure and velocity at the surface of the i^{th} chamber, $p_{S,i}$ and $u_{S,i}$, respectively, in conjunction with backplate boundary condition values. This is shown mathematically as

$$\begin{pmatrix} p_{S,i} \\ u_{S,i} \end{pmatrix} = \begin{pmatrix} T_{11,i} & T_{12,i} \\ T_{21,i} & T_{22,i} \end{pmatrix} \begin{pmatrix} p_{0,i} \\ u_{0,i} \end{pmatrix}. \tag{7}$$

Since $u_{0,i}$ is equal to zero, Eq. (7) reduces to

$$\begin{pmatrix} p_{S,i} \\ u_{S,i} \end{pmatrix} = \begin{pmatrix} T_{11,i} p_{0,i} \\ T_{21,i} p_{0,i} \end{pmatrix}. \tag{8}$$

The normalized specific acoustic impedance for the i^{th} chamber (ζ_i) is then defined as

$$\zeta_i = \frac{p_{S,i}}{u_{S,i}} = \frac{T_{11,i}}{T_{21,i}} = \frac{\cosh(k\Gamma h_i)}{\zeta_C^{-1} \sinh(k\Gamma h_i)}, \tag{9}$$

where transmission coefficients $T_{11,i}$ and $T_{21,i}$ are as defined in Parrott & Jones [6]. Note that h_i is the depth of the i^{th} chamber, Γ is the propagation constant, and ζ_C is the characteristic impedance of the chamber. Assuming the chamber is filled with air, the propagation constant is computed via [6]

$$\Gamma = \sqrt{\frac{\mathrm{J}_0(\mathrm{i}^{3/2}s)}{\mathrm{J}_2(\mathrm{i}^{3/2}s)}}\sqrt{\frac{\gamma}{n_\Gamma}}, \tag{10}$$

where $\mathrm{J}_0()$ and $\mathrm{J}_2()$ are Bessel functions of the first kind of orders zero and two, respectively, and n_Γ is computed using

$$n_\Gamma = \left[1 + \frac{\gamma - 1}{\gamma}\frac{\mathrm{J}_2(\mathrm{i}^{3/2}\sigma s)}{\mathrm{J}_0(\mathrm{i}^{3/2}\sigma s)}\right]^{-1}. \tag{11}$$

The shear wave number (s), Prandtl number (σ^2), and ratio of specific heats (γ) are calculated using

$$s = \frac{d_E}{2}\sqrt{\frac{\rho\omega}{\mu}}, \sigma^2 = \mu\frac{C_P}{\kappa}, \text{and } \gamma = \frac{C_P}{C_V}, \tag{12}$$

where μ is dynamic viscosity of air, κ is thermal conductivity of air, and C_P and C_V are specific heats of air at constant pressure and volume, respectively. The characteristic impedance of air in the chamber is then defined as [6]

$$\zeta_C = \frac{-\mathrm{i}}{\Gamma}\frac{\mathrm{J}_0(\mathrm{i}^{3/2}s)}{\mathrm{J}_2(\mathrm{i}^{3/2}s)}. \tag{13}$$

Note that propagation constant (Γ) and characteristic impedance (ζ_C) formulations are technically for a circular cross section chamber, so corner effects within square chambers are not modeled. For the purposes of this article, the effective diameter of the square chambers is used. This prediction assumption has proven to be a reasonable one for past research studies, at least away from antiresonance [6, 38].

Assuming each chamber has the same effective diameter as well as thermodynamic and viscous quantities, Γ and ζ_C are the same for each chamber. Finally, in order to combine the surface impedance of each chamber into a final effective impedance, one can use

$$\beta = \frac{\Omega}{N_C}\sum_{i=1}^{N_C}\beta_i, \tag{14}$$

where admittances of each chamber, $\beta_i = \zeta_i^{-1}$, are added together, multiplied by the ratio of the acoustically active surface area to total surface area of the sample, Ω, and divided by the number of chambers, N_C. The final effective impedance is then simply the inverse of the final admittance, $\zeta = \beta^{-1}$. This computation is performed separately for each frequency.

4.2. Model 2: simplified radiation impedance included

This model was developed in Schiller & Jones [21] and uses the same general approach as Model 1, but it modifies Eq. (9) to include a radiation impedance term (assumed purely reactive). This is done using a frequency-independent, mass-end correction term. Generically, Eq. (9) extends to

$$\zeta_i = \frac{\cosh(k\Gamma h_i)}{\zeta_C^{-1}\sinh(k\Gamma h_i)} + \mathrm{i}k\delta_i, \tag{15}$$

where δ_i is the mass-end correction term for the i^{th} chamber. The value of the end-correction term is location and chamber-size dependent, derived from assumptions based on source-imaging effects and Ingard's simplified correction for a centered massless piston radiating into a tube of finite cross section [25, 26]. The end correction for a chamber is

$$\delta_i = \begin{cases} \frac{4}{3\pi} d_E(1 - 1.25\sqrt{\phi}) & \text{interior} \\ \frac{4\sqrt{2}}{3\pi} d_E(1 - 1.25\sqrt{\phi}) & \text{edge} \\ \frac{8}{3\pi} d_E(1 - 1.25\sqrt{\phi}) & \text{corner,} \end{cases} \tag{16}$$

where ϕ is the ratio of an individual chamber surface area to the total cross-sectional area of the impedance tube.

The appropriate form in Eq. (16) is selected for each chamber location to determine the corresponding end correction term (δ_i) for the i^{th} chamber, which then gets inserted into Eq. (15) for the surface impedance computation. Every other part of the process is identical to Model 1. As stated earlier, this approach assumes there is no mutual radiation impedance between chambers, so it is only including the added self radiation impedance, where each chamber is assumed to radiate in isolation within the tube. In order to compute mutual radiation impedance between chambers, Model 3 is employed.

4.3. Model 3: full analytical solution

Model 3 uses a transmission-line approach in a similar manner to that used in the previous models. However, since the relative magnitude and phase of each chamber's surface particle velocity is critical to the overall surface impedance, one must now constrain the acoustic pressure at the surface rather than at the backplate. Under the assumption again that nonlinear effects are negligible, and that only plane waves are propagating within the impedance tube, an acoustic pressure constraint is applied just above the liner surface. Although evanescent modes are present right at the surface of the liner due to chamber radiation, for the frequencies considered in this study, they are low in amplitude and strongly decay over a short distance [26]. As a result, the plane wave is still assumed to be dominant a small distance away from the surface. The surface acoustic pressure constraint for the i^{th} chamber is therefore approximated as $p_{S,i} = 1 + 0\mathrm{i}$ (same for every chamber), where as stated before, nonlinear effects are negligible, so the magnitude of the surface acoustic pressure is arbitrary for these sample types. Although not explored in this article, it is possible to assess other surface acoustic pressure constraints, i.e., higher-order dominant modes at the surface, arbitrary pressure distributions, etc.

Knowing that the surface acoustic pressure is approximated to be the same for every chamber due to the plane-wave assumption, one must solve for each chamber's surface particle velocity in order to compute each chamber's surface impedance, with the intent of combining these values at the end for the effective surface impedance of the sample. To do this, a number of assumptions are made. The acoustic particle velocity at the surface of each chamber is assumed to be of uniform distribution throughout the cross section. Additionally, accounting for the radiation impedance in this context is an assumed lumped-element process (valid due to the small change

in distance from position 1 to position S and frequencies assessed in this study), so there is no change of particle velocity, resulting in $u_{1,i} = u_{S,i}$. One can take Eq. (9) (replacing $p_{S,i}$ with $p_{1,i}$) and manipulate for an expression of acoustic pressure just below the surface as a function of surface particle velocity, shown as

$$p_{1,i} = \left(\frac{\cosh(k\Gamma h_i)}{\zeta_C^{-1} \sinh(k\Gamma h_i)} \right) u_{S,i}. \tag{17}$$

It is assumed again that radiation impedance is purely reactive and modeled as a transfer impedance that generates an acoustic pressure change, shown analytically as

$$\zeta_{R,i} = \frac{p_{S,i} - p_{1,i}}{u_{S,i}}, \tag{18}$$

where rearranging this formulation and inserting Eq. (2) for the radiation impedance gives

$$p_{1,i} + \mathrm{i}k\delta_i u_{S,i} = p_{S,i}. \tag{19}$$

If one substitutes Eq. (17) into Eq. (19), the following relation is obtained:

$$\left(\frac{\cosh(k\Gamma h_i)}{\zeta_C^{-1} \sinh(k\Gamma h_i)} \right) u_{S,i} + \mathrm{i}k\delta_i u_{S,i} = p_{S,i}. \tag{20}$$

Recall, Eq. (5) shows that radiation impedance of a given chamber is the combination of its self radiation impedance and mutual radiation impedance with every other chamber in the array, weighted by their particle velocity ratios. This is shown analytically as

$$\zeta_{R,i} = \mathrm{i}k\delta_i = \mathrm{i}k \sum_{j=1}^{N_C} \delta_{ij} \frac{u_{S,j}}{u_{S,i}}, \tag{21}$$

where δ_{ij} is the mutual radiation, mass-end correction term due to the j^{th} chamber, and $u_{S,j}$ is the surface particle velocity of the j^{th} chamber. As stated earlier in the article, self-radiation is included when $j = i$, and the particle velocity ratio is then one. Breaking out the self and mutual radiation terms separately gives

$$\zeta_{R,i} = \mathrm{i}k\delta_i = \mathrm{i}k\delta_{ii} + \mathrm{i}k \sum_{\substack{j=1 \\ j \neq i}}^{N_C} \delta_{ij} \frac{u_{S,j}}{u_{S,i}}, \tag{22}$$

where δ_{ii} is the self radiation, mass-end correction term. This means for the i^{th} chamber, Eq. (20) becomes

$$\left(\frac{\cosh(k\Gamma h_i)}{\zeta_C^{-1} \sinh(k\Gamma h_i)} + \mathrm{i}k\delta_{ii} \right) u_{S,i} + \mathrm{i}k \sum_{\substack{j=1 \\ j \neq i}}^{N_C} \delta_{ij} u_{S,j} = p_{S,i}. \tag{23}$$

This equation is repeated for each chamber in the array. In short, a linear system of equations must be solved to compute surface particle velocities for every chamber simultaneously. This is represented in matrix format as

$$\begin{pmatrix} \frac{\cosh(k\Gamma h_1)}{\zeta_C^{-1}\sinh(k\Gamma h_1)} + \mathrm{i}k\delta_{11} & \mathrm{i}k\delta_{12} & \cdots & \mathrm{i}k\delta_{1N_C} \\ \mathrm{i}k\delta_{21} & \frac{\cosh(k\Gamma h_2)}{\zeta_C^{-1}\sinh(k\Gamma h_2)} + \mathrm{i}k\delta_{22} & \cdots & \mathrm{i}k\delta_{2N_C} \\ \vdots & \vdots & \ddots & \vdots \\ \mathrm{i}k\delta_{N_C1} & \mathrm{i}k\delta_{N_C2} & \cdots & \frac{\cosh(k\Gamma h_{N_C})}{\zeta_C^{-1}\sinh(k\Gamma h_{N_C})} + \mathrm{i}k\delta_{N_CN_C} \end{pmatrix} \begin{pmatrix} u_{S,1} \\ u_{S,2} \\ \vdots \\ u_{S,N_C} \end{pmatrix} = \begin{pmatrix} p_S \\ p_S \\ \vdots \\ p_S \end{pmatrix} \tag{24}$$

where as mentioned before, the right-hand-side vector is the same value for every chamber, i.e., $p_S = p_{S,i}$. Once these particle velocities are found, the surface impedance of each chamber is then computed ($p_S/u_{S,i}$) and combined together via Eq. (14).

The computation of mass-end correction terms is taken from work performed in Ih [27], where terms are derived from acoustic potential formulations assuming massless pistons of various shapes radiating into differently shaped, infinitely-long tubes. The coordinate system for the mass-end correction computation is shown in Figure 6, showing a 5×5 chamber array as example. The full-frequency formulation for a rectangular piston radiating into a rectangular tube is used and shown as [27]

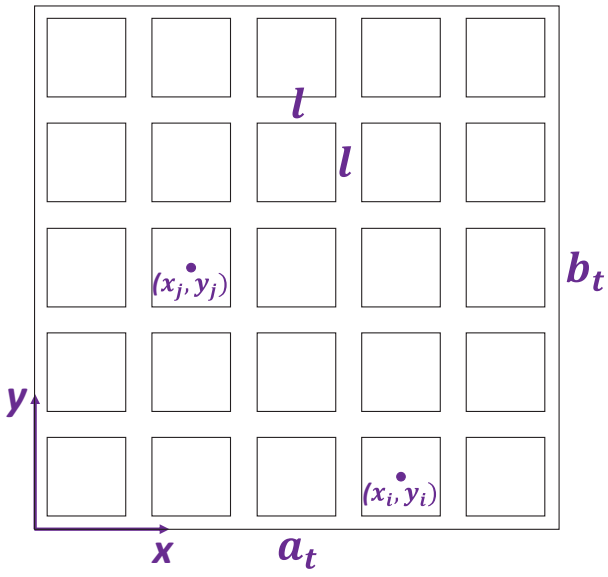

Figure 6: Coordinate system for the mass-end correction calculation.

$$\delta_{ij} = \frac{\mathrm{i}l^2}{a_t b_t}\Bigg(\sum_{m=1}^{\infty}\frac{1}{k_{m0}v_{m0}}G_m^2 H_m H'_m + \sum_{n=1}^{\infty}\frac{1}{k_{0n}v_{0n}}G_n^2 H_n H'_n + \sum_{m=1}^{\infty}\sum_{n=1}^{\infty}\frac{1}{k_{mn}v_{mn}}G_m^2 G_n^2 H_m H'_m H_n H'_n\Bigg), \tag{25}$$

where $v_{m0} = v_{0n} = 0.5$, $v_{mn} = 0.25$, and the axial wavenumber, k_{mn}, is defined as

$$k_{mn} = \sqrt{k^2 - \left(\frac{m\pi}{a_t}\right)^2 - \left(\frac{n\pi}{b_t}\right)^2}. \tag{26}$$

Mode orders associated with the rectangular tube are defined as (m, n), l is the side length of the chamber square cross section, and a_t and b_t are the width and height of the impedance tube, respectively. The G_m and G_n terms are defined as

$$G_m = \frac{\sin\left(m\pi l/2a_t\right)}{m\pi l/2a_t}, G_n = \frac{\sin\left(n\pi l/2b_t\right)}{n\pi l/2b_t}, \tag{27}$$

while the H_m, H_n, H'_m, and H'_n terms are defined as

$$H_m = \cos\left(\frac{m\pi x_i}{a_t}\right), H_n = \cos\left(\frac{n\pi y_i}{b_t}\right), H'_m = \cos\left(\frac{m\pi x_j}{a_t}\right), \text{ and } H'_n = \cos\left(\frac{n\pi y_j}{b_t}\right), \tag{28}$$

where (x_i, y_i) and (x_j, y_j) are center surface coordinates of the i^{th} and j^{th} chambers, respectively. If the frequencies of interest are sufficiently below the cuton frequency of the first higher-order mode in the tube, a low-frequency approximation can be used, where $k \approx 0$ is assumed in the axial wavenumber computation. This is advantageous in terms of computational time when computing impedance for a large number of frequencies, as k_{mn} is assumed constant with frequency. Therefore, two variants of Model 3 are analyzed. The low-frequency approximation approach is denoted as Model 3a, while the full formulation is denoted as Model 3b.

The computation of this mutual radiation, mass-end correction term for the i^{th} chamber is paired with every chamber associated with the sample, including itself (self radiation impedance: $j = i$). This calculation is performed for every chamber in the sample, which results in an $N_C \times N_C$ array of end correction terms that get inserted into the system of equations shown in Eq. (24). In order to identify a sufficient number of modes to use in the computation, a study is conducted where predictions are made for every sample, starting at $(m, n) = (5, 5)$ and going up in increments of five. This is done until the L_2 norm (definition described later in this article) between the current and previous predictions (cumulative for all samples) is below 0.01. This helps identify convergence while also keeping computational times low. The result of the convergence study demonstrates that a mode index of 30 is required in both directions, i.e., $(m, n) = (30, 30)$, which is used for every Model 3 prediction shown in this article. This convergence study is done for both Models 3a and 3b, yielding the same findings.

5. Experimental vs. Prediction Results

Comparisons are made between prediction and experimental data using the various impedance models. Normalized reactance spectra are the focus of these comparisons. For open chambers that are sufficiently wide in cross section ($\geq 0.25''$), resistance due to losses from the chamber walls are quite low. Figure 7 shows Model 1 predictions for a select few cases. When the sample is constant depth (Sample 1), all chambers radiate in phase with one another, and radiation impedance is nearly negligible. Figure 7 shows near perfect agreement between model and experiment for Sample 1. However, differences arise when variable-depth chambers are assessed. Upon analyzing Samples 2 and 5 in Figure 7, Model 1 is not adequately predicting reactance, showing a clear shift to the right in prediction relative to experiment, as well as failing to predict more-detailed behavior due to mutual interaction effects. Radiation impedance clearly needs to be accounted for if a sufficiently accurate prediction is to be made. In addition to this, predicted antiresonant spikes are larger in magnitude compared to experiment, indicating that predicted dissipation due to chamber walls is slightly different than experiment. This is seen throughout this section for every model presented. A likely reason for this, as mentioned earlier, is that the impedance formulation being used assumes wave propagation through a circular cross section chamber, not square. So although an effective diameter for the square chamber is being used in the model, acoustic viscothermal differences due to corners, for instance, are not accounted for in the wave propagation.

Model 2 is used to predict impedance of the same two variable-depth samples that are used for Model 1 validation (Samples 2 and 5). Figure 8 shows this comparison. The prediction for Sample 5 is significantly improved relative to Model 1, although more accuracy is still needed. Sample 2, on the other hand, shows similar errors as Model 1, but this is not surprising given the chamber layout of Sample 2 and the assumption of no mutual radiation. Because of this mutual-radiation assumption, Model 2 tends to overpredict radiation impedance, hence a general shift to the left in prediction relative to experiment.

Figure 9 shows experimental reactance of Samples 2 and 5 relative to Model 3a predictions. Excellent agreement is now seen across the entire frequency range for both samples. The low-frequency approximation of the formulation appears to do a satisfactory job. Although emphasis of the article is on reactance modeling, resistance is also predicted well, as seen in Figure 10. Note that resistance is inherently included when L_2 norm computations are shown later in this article.

As mentioned earlier, since this model relies on an acoustic pressure constraint near the surface with constant magnitude and phase for every chamber, the computed acoustic particle velocities are driving impedance changes between chambers. Figure 11 shows computed particle velocities for select chambers associated with a constant-depth (Sample 1) and variable-depth (Sample 5) sample. For the purposes of more realistic particle velocity magnitudes, the surface acoustic pressure constraint has been temporarily lowered to an SPL near 95 dB, like the experiment. Results illustrate the effect of radiation on the chambers. When the sample is constant depth (Sample 1) and radiation effects are negligible, spectra are fairly smooth, with the root-mean-square (RMS) particle velocity peaking at resonance. Relative to the zero phase angle enforced for the surface acoustic pressure, the particle velocity phase angle quickly changes from 90° to -90° as the spectrum crosses the resonant frequency, as one would expect for a single chamber with a rigid backing on one side [26]. These spectra are the same for every chamber in Sample 1.

The results for Sample 5, however, demonstrate much more complex results due to varying

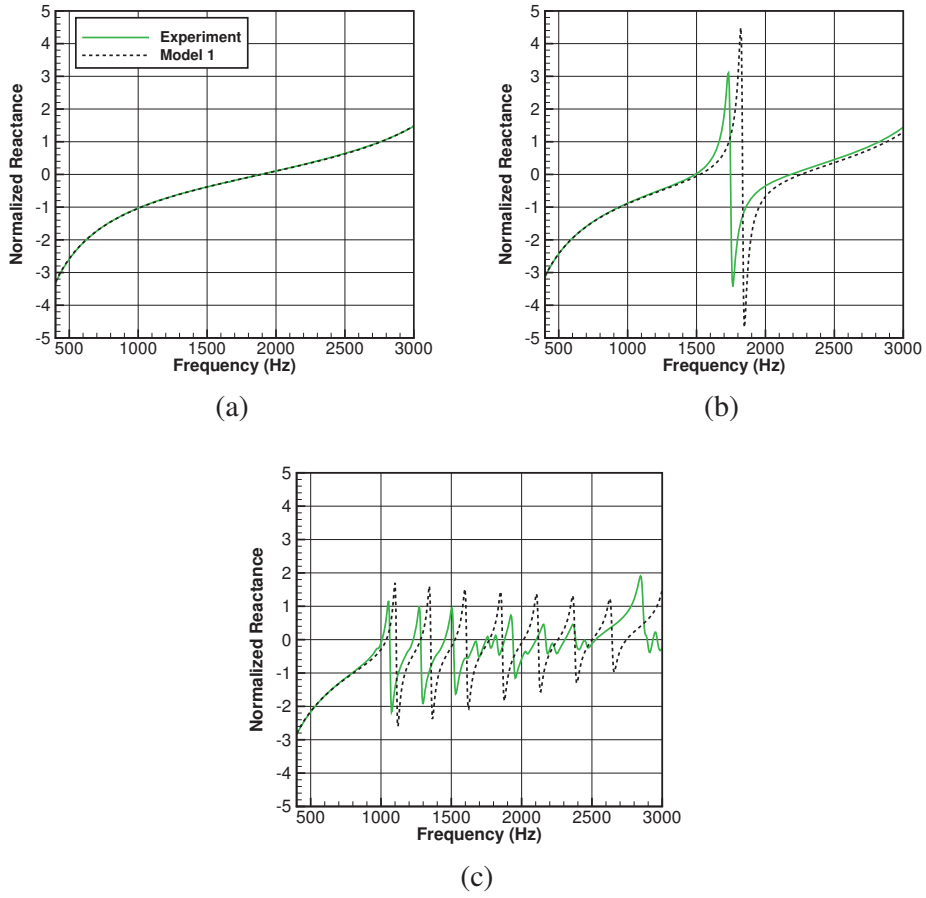

Figure 7: Experimental reactance data (green) compared to Model 1 predictions (dashed black) for (a) Sample 1, (b) Sample 2, and (c) Sample 5, showing the need for radiation impedance inclusion.

chamber depths. Figure 11 shows results for chambers 1, 3, 5, and 7 within the Sample 5 chamber array (within the first seven chambers going left to right, down to up – see Figure 4). RMS velocity peaks at different frequencies for different chambers, as expected due to different depths, but one can see complex interference patterns associated with each spectrum due to chamber radiation. Without chamber radiation included in the model, spectra would look more like a series of smoother curves similar to that of Sample 1. This complex behavior also extends to the phase angles, where this time only chambers 1 and 7 are included to make the plot more readable in Figure 11. Although phase angles still largely hover around 90° or -90° depending on the resonant frequencies of each chamber, radiation effects are causing shifts in the phase angle, sometimes drastically.

To gain more insight on improvements between Models 2 and 3a, comparisons are also made

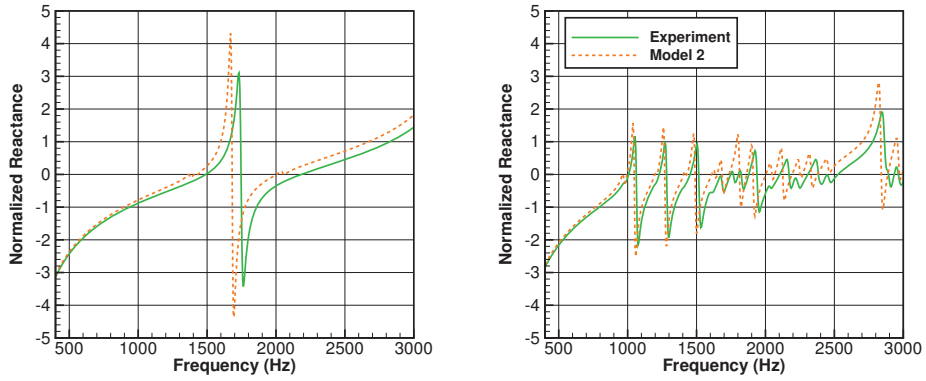

Figure 8: Experimental reactance data (green) compared to Model 2 predictions (dashed orange) for (a) Sample 2 and (b) Sample 5, indicating higher accuracy than Model 1 but with improvements still needed.

using Sample 9, as the "unlikes grouped" case should adhere best to assumptions laid out in Model 2 due to unlike depths placed next to one another. The results are shown in Figure 12, where Model 3a again outperforms Model 2 across the entire frequency range. Model 3b, being the complete formulation, should improve accuracy even further. This assumption, however, is not quite true. Figure 13 shows a comparison of model accuracy for Samples 6 and 8 using Models 3a and 3b. It appears from these particular samples that Model 3b slightly overpredicts the spectra, although accuracy is still very good. This would suggest that Model 3a does a better job of predicting reactance spectra despite its low-frequency assumption. However, this is sample dependent.

Figure 14 shows another comparison of Models 3a and 3b, this time using Samples 7 and 11 for validation. For these samples, there are marginal improvements made at higher frequencies when Model 3b is used, which is different than when Samples 6 and 8 were used for comparison. More will be discussed on this in the next section.

6. L_2 Norm Analysis

To achieve a broader understanding of the accuracies of each model, an L_2 norm is computed for each prediction method, using each sample individually as well as one cumulative metric. The L_2 norm is calculated using

$$L_2 = \sqrt{\frac{\sum_{i=1}^{N_{\mathrm{TP}}} (\zeta_{P,i} - \zeta_{E,i})(\zeta_{P,i} - \zeta_{E,i})^*}{\sum_{i=1}^{N_{\mathrm{TP}}} \zeta_{E,i}\zeta_{E,i}^*}}, \tag{29}$$

where $\zeta_{P,i}$ is the predicted impedance for a given data point (i), $\zeta_{E,i}$ is the experimental impedance for the i^{th} point, and N_{TP} is the total number of data points. The number of data points is either the

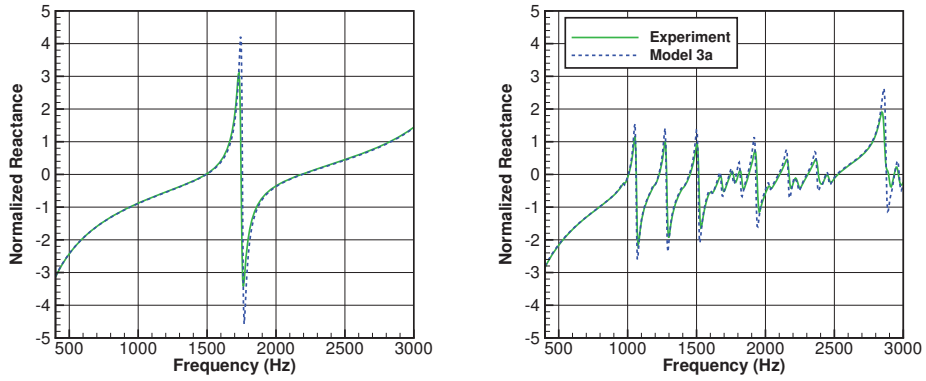

Figure 9: Experimental reactance data (green) compared to Model 3a predictions (dashed blue) for (a) Sample 2 and (b) Sample 5, indicating accuracy across the entire frequency range for both samples.

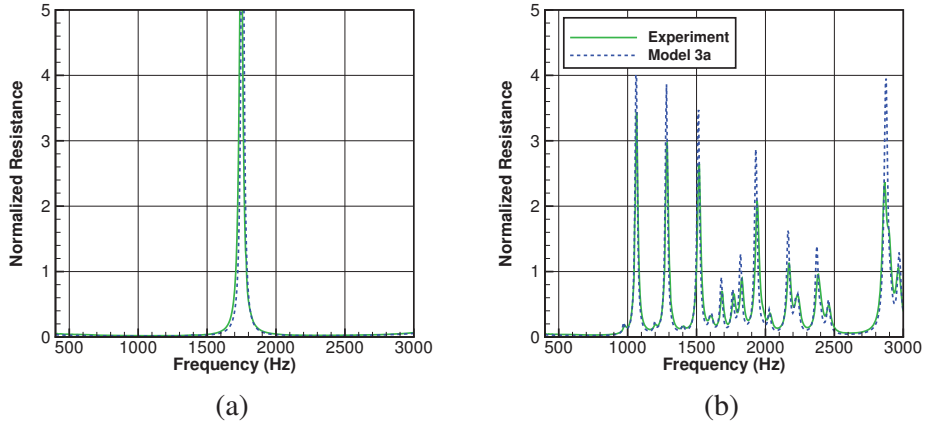

Figure 10: Experimental resistance data (green) compared to Model 3a predictions (dashed blue) for (a) Sample 2 and (b) Sample 5, indicating accuracy across the entire frequency range for both samples.

total number of frequencies per sample, or the total number of frequencies per sample multiplied by the number of samples if one cumulative metric is desired. Jones et al. [4] applied a similar process to quantify impedance predictive accuracy.

L_2 norms derived from finite-element results are also used as a comparative point to the other models. Actran TM [39] is utilized, particularly the low-reduced-frequency assumption for viscothermal wave propagation in ducts [40]. Note that this is different than the low-frequency assumption assumed in Model 3a, as the low-reduced-frequency assumption is more concerned with large acoustic wavelengths relative to chamber cross sections and acoustic boundary lay-

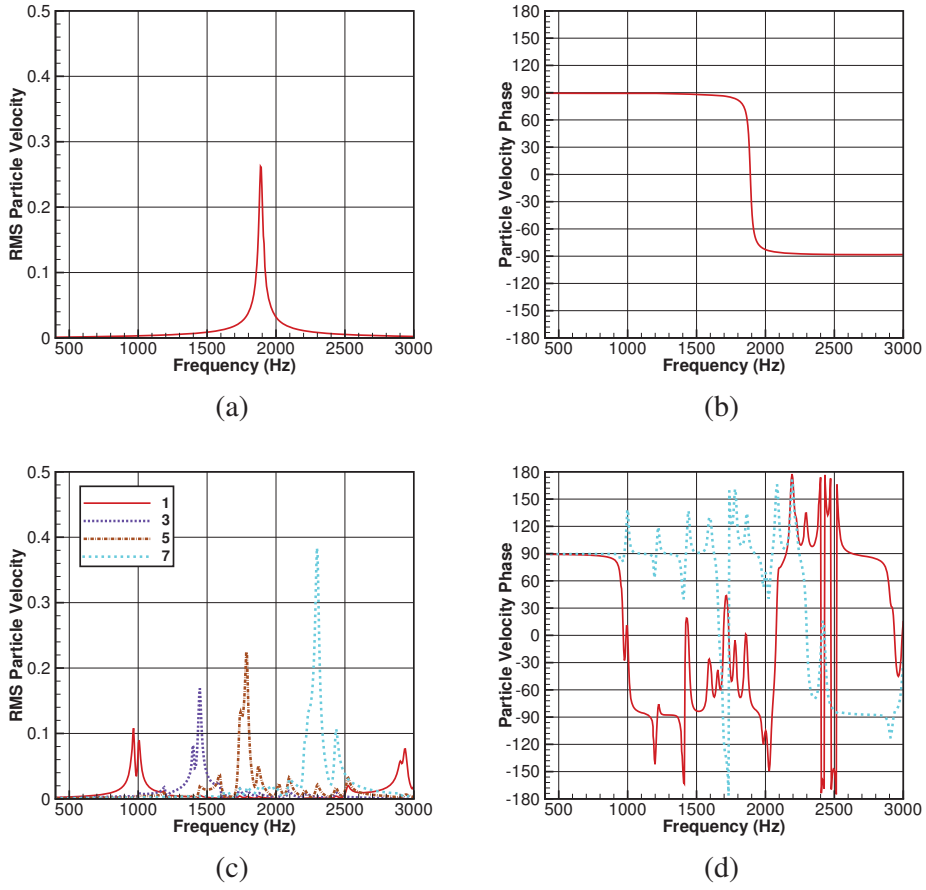

Figure 11: Computed acoustic particle velocities for Sample 1 ((a) root-mean-square amplitude (m/s) and (b) phase angle in degrees) and Sample 5 ((c) root-mean-square amplitude (m/s) and (d) phase angle in degrees) using Model 3a. Sample 5 (c and d) contains spectra for multiple chambers (shown as different colors).

ers present. In order to compute surface impedance within Actran TM, samples are explicitly modeled in the impedance tube environment, effectively mimicking the NIT microphone layout, using the two-microphone method (as discussed previously) to capture results. Radiation impedance is already accounted for in this manner, but it is also more computationally expensive relative to the other models.

Great care is taken to minimize computational time of the finite-element simulations while still producing accurate results. This includes modeling a reduced section of the NIT length, as well as optimizing the mesh so that there is increased refinement near the chamber surfaces to capture higher-order evanescent modes that may affect surface impedance. Note that further refinements to the mesh do not significantly impact impedance results, so the mesh is coarsened out away from the chamber surfaces. Numerous grids were assessed for accuracy, including full

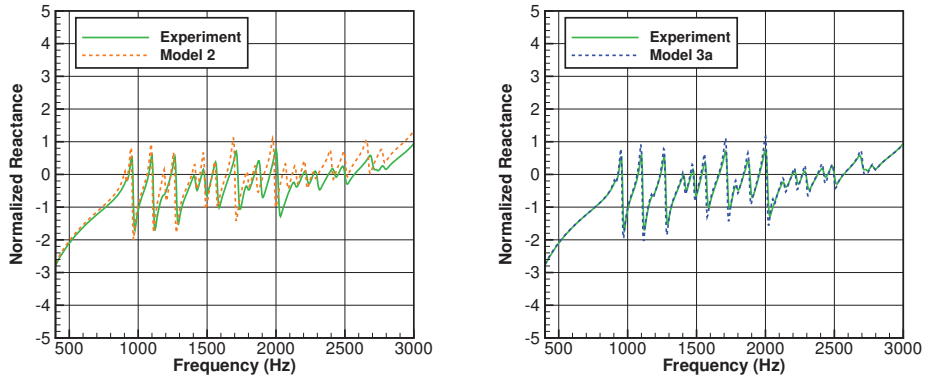

Figure 12: Comparison of (a) Model 2 (dashed orange) and (b) Model 3a (dashed blue) predictions using Sample 9 experimental reactance data (green). Model 3a demonstrates improved modeling across the entire frequency range.

refinement of the entire computational domain, but only refinement near the chamber surface was necessary.

Figure 15 shows results of the L_2 norm study. Sample 1 has been excluded from the analysis, as only Model 1 is needed for the prediction. Model 1 is the least accurate model, as expected. Model 2 shows a sizable improvement, yielding an almost 40% improvement in the L_2 norm cumulative metric relative to Model 1. Errors are further reduced by Models 3a and 3b, as well as the finite-element simulations, where these methods are all fairly close in accuracy. Model 3b exhibits the lowest error, at least for the cumulative metric. The L_2 norm cumulative metric is reduced by almost 75% when Model 3b is used, relative to Model 1. Model 3b also yields an accuracy improvement of almost 60% compared to Model 2. Model 3b seems to exhibit the least variability in the L_2 norm metric across the different samples. Models 3a and 3b produce sizable improvements in impedance accuracy, and for the majority of samples, Model 3a yields the lowest L_2 norm, often outperforming Model 3b. Model 3b only outperforms Model 3a at Samples 4, 7, and 11. There are error spikes for Model 3a using Samples 7 and 11 in particular, suggesting that larger chamber diameters are playing a role in reducing the accuracy of Model 3a. Conversely, some of the lowest errors computed with Model 3a are associated with the smaller chamber diameters (i.e., Sample 4, 0.275″, and Sample 10, 0.300″). The increased errors associated with larger chamber diameters are likely due to an enhancement of errors connected with the low-frequency assumption. As was shown earlier, end correction terms scale roughly with the side length of the chamber, l, so as predicted radiation impedance goes up, low-frequency-assumption errors likely go up as well.

Except for Sample 7 where chambers are larger, the low-frequency approximation (Model 3a) outperforms the full formulation (Model 3b) when partitions between chambers are thin (0.025″). Interaction effects between radiating chambers are strong in this configuration, and Model 3b tends to slightly overpredict the radiation impedance. The most likely explanation for this is that printed sample geometries are slightly different than what was targeted. As mentioned earlier in the article, 3D-printed sample dimensions are typically within ±0.005″ of the target,

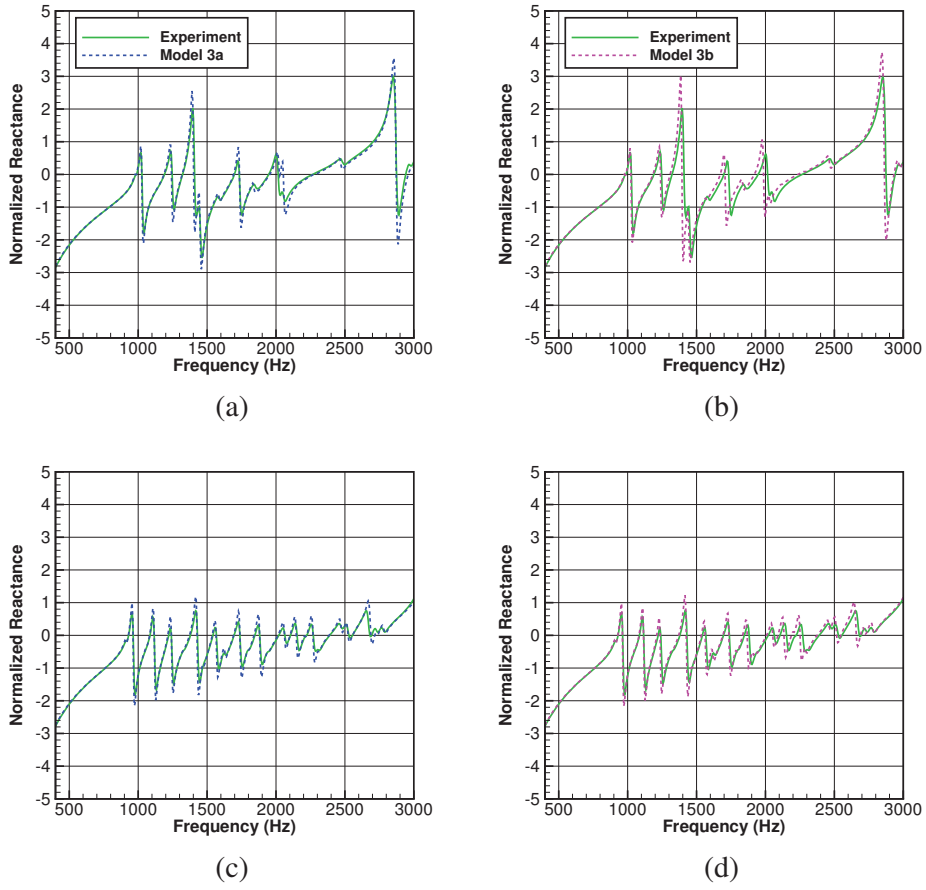

Figure 13: Comparison of Models 3a (dashed blue) and 3b (dashed pink) predictions to experimental reactance data (green). Model 3a predictions are done for (a) Sample 6 and (c) Sample 8, while Model 3b predictions are also done for (b) Sample 6 and (d) Sample 8. Model 3a demonstrates slightly better accuracy for these samples.

and sometimes these tolerances are modified further if resin bleed from the laser occurs, which certainly could have happened for the partitions since they are so thin. There were no detailed geometric measurements performed on these samples, but some quick estimations of the partition thicknesses using calipers indicated that they are close to the targeted design, but possibly slightly thicker than desired. Some small differences in partition thickness could slightly alter mutual radiation impedance, and if they are thicker than expected (which also means that chamber effective diameters are a bit smaller), it would stand to reason that Model 3b may slightly overestimate. This would also explain why Model 3b is typically about as good or better than 3a when partitions are thicker, where resin bleed is less of an issue. That being said, error differences for all samples are quite small between Models 3a and 3b; one can review Figures 13 and 14 to see that minimal differences in impedance show up in L_2 norms more drastically, especially

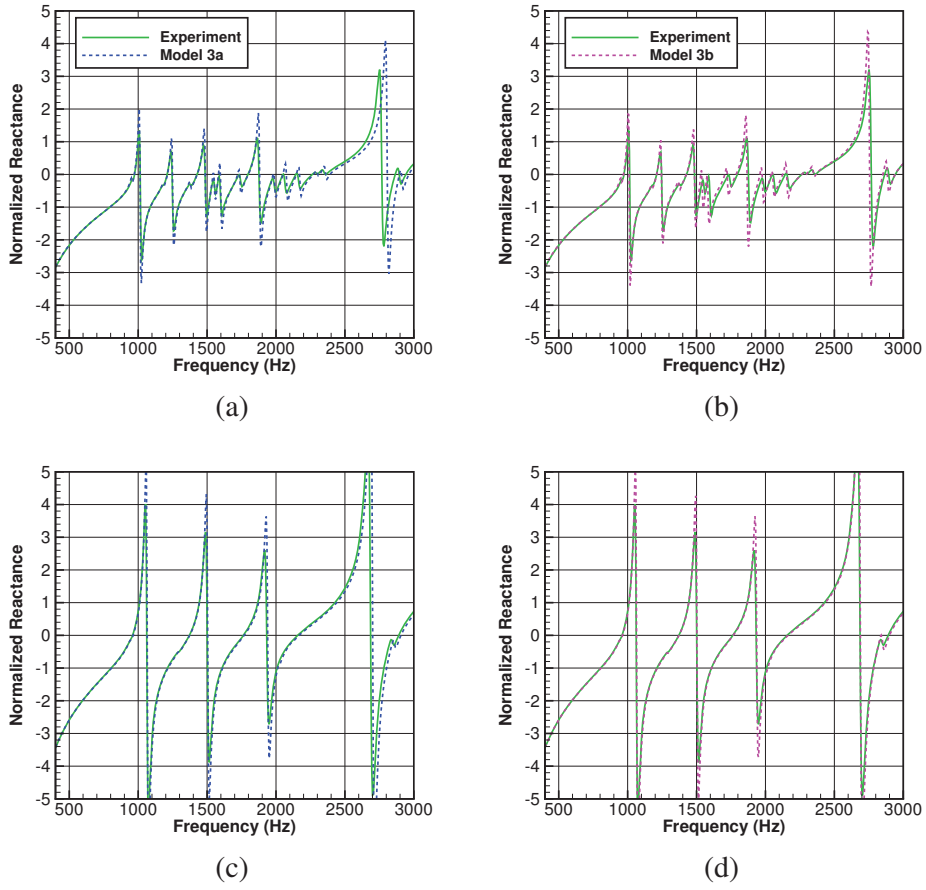

Figure 14: Comparison of Models 3a (dashed blue) and 3b (dashed pink) predictions to experimental reactance data (green). Model 3a predictions are done for (a) Sample 7 and (c) Sample 11, while Model 3b predictions are also done for (b) Sample 7 and (d) Sample 11. Sample 11 experimental data are taken, with permission, from Galles et al. [12], a work of the U.S. Government. Model 3b demonstrates marginally improved accuracy for these samples.

if there are slight shifts between prediction and experiment near antiresonance. The intent of the current study is to assess errors over the entire frequency range, but future efforts could filter out the sharp antiresonant discontinuities. Overall, Models 3a and 3b produce vast improvements in accuracy, comparable to finite-element methods. Computational times need assessing to determine usability of methods in a setting where quick iterations or a large number of predictions are required. This is shown in the next section.

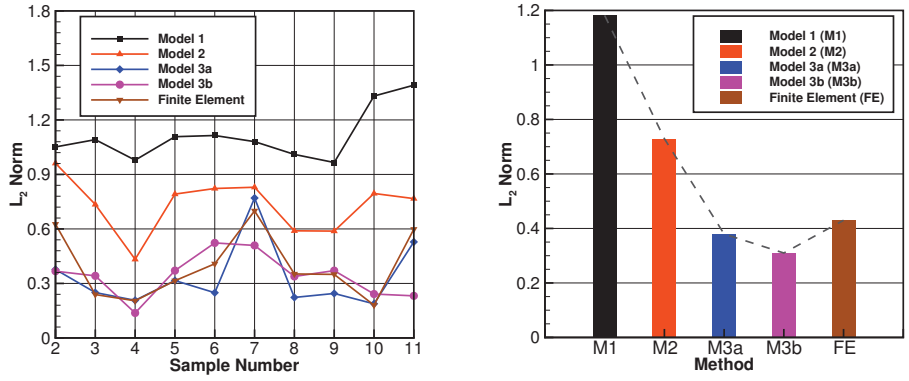

Figure 15: L_2 norm comparison (a) per sample, as well as (b) for all samples cumulatively.

7. Computational Time Comparisons

Model efficiency is a critical comparative point between methods. It is not necessarily desirable to have a more accurate model if computational times are not suitable for the particular application. Design studies in particular require efficient models when coupled with optimization routines. To assess code efficiency, wall-clock time (real time from start to finish of executable run) is captured for each model. As this can vary slightly every time the program is run, each model is executed five times for every sample, with wall-clock times averaged together. As mentioned earlier, Models 1–3b are all Fortran codes, compiled the same way, and written in a manner to be very similar to one another. This computational comparison approach should be sufficient for a general understanding of the trends.

Table 2 shows average computational times per frequency for computing the surface impedance of Samples 2–11, using all models and variants. There are 512 frequencies per sample computed using each model to derive the values shown in Table 2. An average time value is calculated for each model and sample (based on the five separate runs described earlier), and then values for all samples per model are averaged together to compute the numbers shown in Table 2. Reading from left to right in Table 2, the models increase in computational time.

Table 2: Computational times (seconds) per frequency based on wall-clock times averaged over multiple runs and all samples.

Model 1	Model 2	Model 3a	Model 3b
4.56E-05	4.60E-05	1.22E-04	1.29E-03

Models 1 and 2 are clearly the most efficient models, operating at nearly the same computational times. Given the significant increase in accuracy achieved by implementing Model 2, its advantage over Model 1 is clear. However, Model 3a is also quite efficient, only taking ~2.5 times longer to run than Models 1 and 2. This is accompanied by a vast improvement in accuracy. Although 2.5 times is not insignificant, it is a multiplier of a very small time value. Model

3a is computing at a rate of $\sim 10^{-4}$ seconds per frequency. As mentioned earlier, it is feasible that this time could be reduced further if less modes are included in the computation. However, these computational times are also chamber-array-size dependent, as Models 3a and 3b must compute $\sim N_C^2$ operations, while Models 1 and 2 compute $\sim N_C$ operations. Although not shown in this article, computational times for Samples 7 and 11 are shorter than others for Model 3a, and this is because there are less chambers to loop through. A larger chamber array would consequently increase computational time.

Model 3b takes roughly an order of magnitude longer to run than Model 3a but is still operating at $\sim 10^{-3}$ seconds per frequency. Although not shown in the results presented here, Model 3b demonstrates fairly consistent computational times for different chamber layouts, indicating that the added frequency dependence of Model 3b (relative to 3a) is the main driver for computational expense. Perhaps the most important finding, however, is the comparison to finite-element methods. Although not documented in the same way as Models 1–3b, the finite-element predictions used for the L_2 norm comparisons generally took a few seconds per frequency to run for this particular study. This indicates that Models 3a and 3b are orders of magnitude quicker to run while being just as accurate. Finite-element computations still have the advantage though in terms of arbitrary designs and environments, as Models 3a and 3b are set up for very specific cases. However, finite-element methods also suffer from added preparation time, having to regrid a new geometry for every sample. This issue is further enhanced when optimization schemes for design are implemented. Models 3a and 3b, on the other hand, only need updated parameters to run a new iteration.

8. Application to Narrow Chamber Widths

As mentioned earlier, the influence of radiation impedance on open-variable-depth chambers is lessened as the chamber width gets smaller. Typically for aerospace applications, if the variable-depth liner is composed of wider chambers, a perforated facesheet is placed on top to provide sufficient resistance and mitigate drag and liner self noise. The facesheet holes also act as radiators, and similar modeling as shown in this article can also be applied to configurations including facesheets. There are added difficulties with this though, such as modeling radiation on both sides of the facesheet, as well as relying on an accurate prediction of the facesheet hole transfer impedance. If the chambers are narrow in width ($<0.1''$), the liner provides sufficient resistance for noise absorption due to viscous losses from the chamber walls, and the chamber widths are small enough to lessen aerodynamic drag and liner self noise impact [8]. Acoustic liners of this type have been studied previously and are the subject of a possible future static engine test [41].

Due to the narrow chamber widths, radiation effects are greatly reduced for this type of liner. This is coupled with increased resistance, effectively smoothing out the sharpness of the antiresonant peaks, making them less distinct. However, radiation impedance is a function of the free-space wavenumber (k), meaning that radiating chambers influence impedance more greatly at higher frequencies. For chambers of this size in the NIT (where frequencies only go up to 3000 Hz), effects are minimal. Acoustic liners within engine nacelles often need to absorb noise effectively out to 6000 Hz though, where radiation effects are stronger. It is in this higher frequency range where narrow chamber, variable-depth liners may benefit from improved radiation impedance modeling.

Before modeling narrow chamber, variable-depth liners, a constant-depth liner of narrow chambers is first modeled and compared to experimental data, using Model 1 and a swept-sine tonal excitation of 100 dB. To accomplish this, the CSQ3 liner from previous publications [42]

is used. This sample is a 19 × 19 array of 0.05″ × 0.05″ square chambers, each at a depth of 3″. Figure 16 shows the results, where prediction spectra have been extrapolated out to 6000 Hz. Good agreement is seen between experiment and prediction, although there are some slight discrepancies, likely due to the experimental sample and assumed geometry having slightly different partition thicknesses. The resistance spectra is also shown to be of relatively sufficient magnitude for proper absorption (~0.5) away from the antiresonant regions, demonstrating one of the benefits of narrow chamber designs.

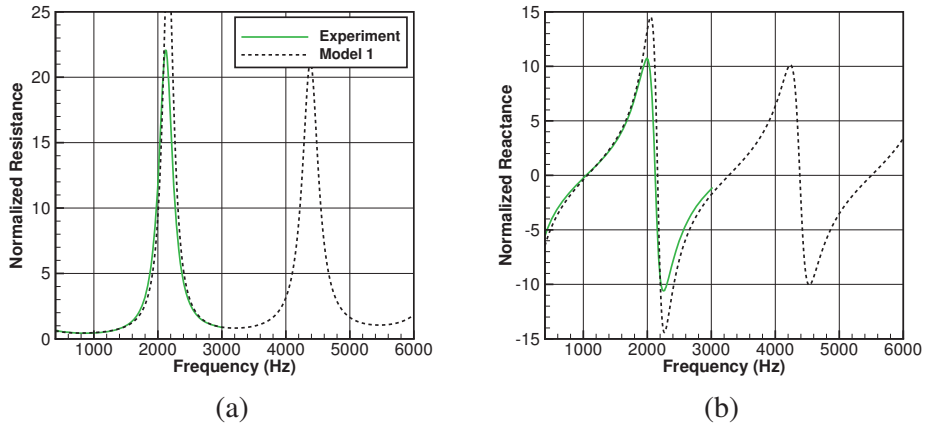

Figure 16: CSQ3 experimental (a) resistance and (b) reactance (green) compared to Model 1 (dashed black) predictions, where prediction data have been extrapolated out to 6000 Hz.

To assess the impact of modeling radiation impedance for narrow chamber, variable-depth liners, a small computational study is performed, comparing predicted impedances between Models 1 (no radiation included) and 3a (radiation included with low-frequency assumption) for four relevant liner designs. The validity of using the low-frequency assumption at these higher frequencies is discussed later in this article. The chamber widths of these virtual samples (0.05″ and 0.10″) are similar to designs outlined in Nark et al. [41]. The desired target frequency range this time is assumed to be 800–6000 Hz, and like before, unique chamber depths are selected so that resonances are distributed fairly equally. For these two chamber widths, the number of unique chamber depths is either five or twenty-five, making the total number of virtual samples four. These chamber depth layouts are selected to strongly vary the spacing of antiresonances for each chamber as well as radiating-phase relationship between each. Also, for narrow chamber, variable-depth liners, more variation in chamber depth is typically employed, since more chambers can be packaged in a small amount of space, hence why twenty-five unique chambers are of interest. The geometry for the four samples is shown in Table 3, and the depth layouts are shown in Figure 17, showing the size differences between the different virtual samples.

The partitions between chambers have also been set to be 0.025″ thick. Like previous samples, unique chamber depths are placed in descending order, going left to right, bottom to top. While these samples could have been printed and tested, the NIT does not allow for the frequencies of interest in this study (up to 6000 Hz). The intent of this exercise is to demonstrate differences in the prediction spectra, where the inclusion of radiation impedance is the primary discriminator

Table 3: Sample geometries for narrow-chamber liner samples.

Sample Name	Chamber Layout	Chamber Side Length	Partition Thickness	Chamber Depths
V1, V2	Descending	0.05″, 0.10″	0.025″	(1) 2.037″ (2) 1.340″ (3) 0.999″ (4) 0.796″ (5) 0.661″
V3, V4	Descending	0.05″, 0.10″	0.025″	(1) 3.396″ (2) 2.830″ (3) 2.425″ (4) 2.122″ (5) 1.886″ (6) 1.698″ (7) 1.543″ (8) 1.415″ (9) 1.306″ (10) 1.213″ (11) 1.132″ (12) 1.061″ (13) 0.999″ (14) 0.943″ (15) 0.894″ (16) 0.849″ (17) 0.808″ (18) 0.772″ (19) 0.738″ (20) 0.707″ (21) 0.679″ (22) 0.653″ (23) 0.629″ (24) 0.606″ (25) 0.585″

between the two prediction models.

In order to predict the impedance of these samples, modifications to the analytical setup are implemented. To maintain the low-frequency assumption, the NIT environment is no longer modeled. Rather, smaller impedance tubes are modeled to keep frequencies below the first higher-order cuton mode. A 5×5 chamber setup is implemented for both chamber width cases, meaning that impedance tubes of $0.375'' \times 0.375''$ and $0.625'' \times 0.625''$ are used for chamber widths of $0.05''$ and $0.10''$, respectively. Due to the smaller impedance tubes and chamber cross sections being modeled, Model 3a is assumed adequate, and therefore Model 3b is not used here. Results for the twenty-five unique depths are shown in Figure 18, while the five unique depths are shown in Figure 19.

Differences between predictions are smaller than what was seen earlier in this article for the wider chambers (due to radiation impedance scaling larger with increased chamber width), but it is clear that accounting for radiation effects yields different results, even at these small sizes. The antiresonances are greatly reduced when there are more unique chamber depths (and due to smaller chamber widths in general), as the resonances of some are mitigating the antiresonances of others. This is seen in Figure 18, where twenty-five unique depths are used. Reducing the sharpness of these antiresonances due to increased chamber dissipation mitigates the differences between the two predictions (since the magnitudes of the antiresonances are smaller and appear more flattened out), although there are still distinct differences above 4500 Hz, as expected due to the increasing importance of radiation impedance at higher frequencies. When the number of unique depths drops to five (as shown in Figure 19), antiresonances are more impactful (as they are more distributed in frequency), and differences are a bit more clear, especially for the $0.1''$ chamber width case.

In general, the larger chamber width case ($0.1''$) produces more distinct differences, especially at higher frequencies, and this is expected due to the enhanced radiation effects. Differences are minor though compared to the larger chamber widths assessed earlier in this article. It is advisable to use Model 3a for narrow chamber, variable-depth liners, especially when the chambers are a little wider than conventional facesheet holes. Given the marginal computational cost increase associated with Model 3a relative to Models 1 or 2, the added accuracy is justifiable, as

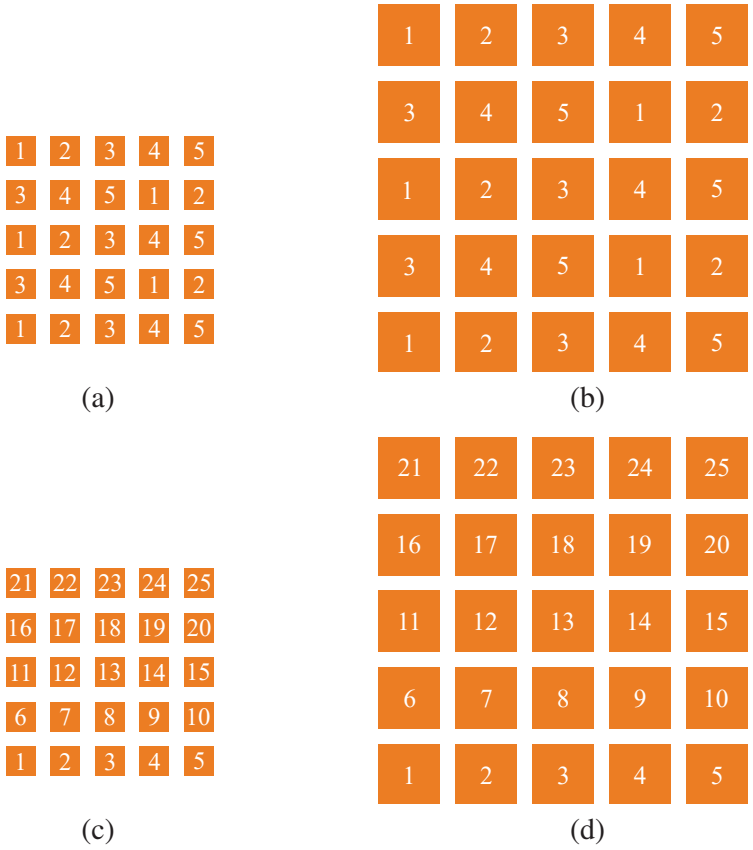

Figure 17: Narrow-width chamber depth layouts for (a) Sample V1, (b) Sample V2, (c) Sample V3, and (d) Sample V4.

impedance differences are distinct enough to possibly produce slight changes in predicted attenuation performance. Grazing flow, however, will gradually diminish this radiation impedance as the flow speed goes up [20]. If the narrow-chamber acoustic liner is designed for high grazing-flow speeds, it may actually be a better strategy to design the liner with Model 1 (no radiation included), but when verifying the performance in a no-flow impedance tube, use Model 3a to validate the design. For lower flow speeds, as mentioned earlier, it may be necessary to adjust the no-flow radiation impedance model shown in this article with empirical adjustments to quantify the reduction in radiation effects.

9. Summary and Next Steps

A variety of surface impedance models, primarily designed for open-variable-depth chambers in the absence of grazing flow, were documented and compared. A new modeling approach, included within these models, takes into account the self and mutual radiation impedance of each chamber, using full and low-frequency-approximation formulations. This method constrains

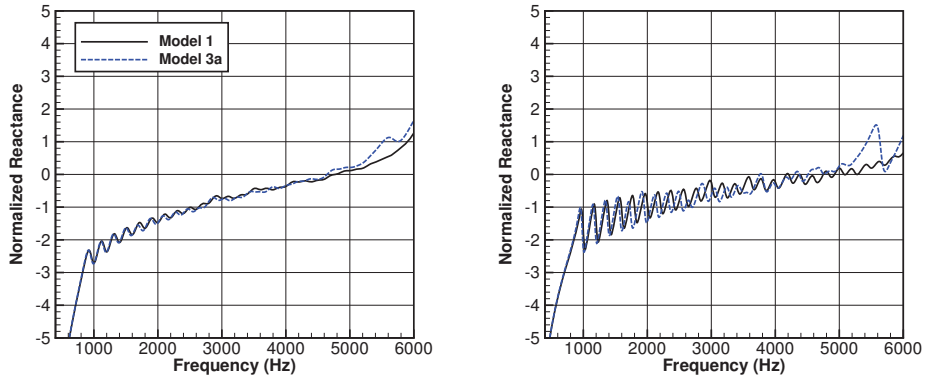

Figure 18: Predicted reactance data for (a) Sample V3 (0.05″ chamber width) and (b) Sample V4 (0.10″ chamber width), using Models 1 (black) and 3a (dashed blue).

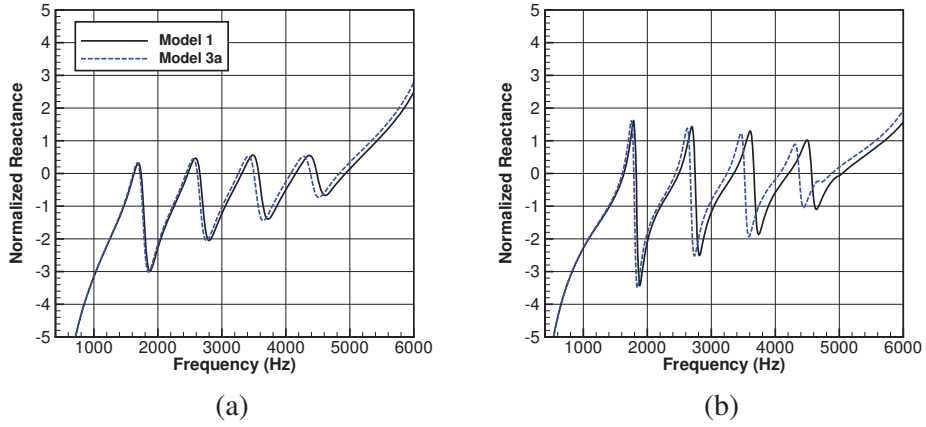

Figure 19: Predicted reactance data for (a) Sample V1 (0.05″ chamber width) and (b) Sample V2 (0.10″ chamber width), using Models 1 (black) and 3a (dashed blue).

the surface acoustic pressure for every chamber (magnitude and phase), constructs a system of equations, and solves for the surface particle velocities of each chamber, thereby computing surface impedance of all chambers simultaneously. Previous literature [27] is used to accurately compute mass-end correction terms for every chamber. An effective impedance for the entire surface is then calculated based on conventional methods.

A variety of open-variable-depth chamber samples were designed, 3D-printed, and tested in a normal-incidence impedance tube as validation data for the models. Comparisons showed that radiation effects are important to model for these types of samples. The new approach

effectively captured radiation impedance for all samples considered. Accuracy was as good as higher-fidelity techniques such as finite-element methods. A computational efficiency study also showed that this approach is orders of magnitude quicker to run than finite-element methods.

The low-frequency-approximation model variant (Model 3a in this article) computed results that were highly accurate and computationally efficient, yielding slightly higher errors when chambers were larger in diameter ($\geq 0.4''$). Using Model 3a resulted in an L_2 norm (cumulative error metric) improvement of almost 70% relative to Model 1 (no radiation impedance modeled) and almost 50% improvement relative to Model 2 (previous model used to account for radiation impedance). This was in conjunction with a computational time per frequency of $\sim 10^{-4}$ seconds, and depending on the needed accuracy, this could be lowered further if less modes were included or mass-end correction calculations were simplified (e.g., some chambers have negligible impact on others and can likely be ignored).

Models 1 and 3a were used to predict the impedance of four narrow chamber, variable-depth liners (chamber widths of $0.05''$ and $0.10''$) to assess the importance of including radiation effects for these liner types. These predictions were performed up to 6000 Hz, as radiation impedance is more significant at higher frequencies, and typical liners within aircraft engine nacelles need to provide performance up to these high frequencies. Differences between model predictions were minor, but distinct enough at higher frequencies that radiation effects should be included within the impedance modeling. If the liner designs are meant for high-speed grazing flows (such as within an aircraft engine nacelle), it is likely best to design the liner assuming no radiation effects (Model 1) but include these effects (Model 3a/3b) when verifying performance in a no-flow impedance tube.

It is recommended to use Model 3a for variable-depth liner modeling to more accurately account for radiation effects while keeping computational times low. Model 3b may be desired for larger radiators (such as larger chamber diameters). This impedance modeling approach can be extended to variable-depth acoustic liners with a facesheet in a no-flow environment, although typically the impact of out-of-phase radiators should be lessened as facesheet holes are much smaller radiators compared to chambers. However, novel facesheet designs (such as hole-clustered layouts [30] and variable-geometry perforation paths [32]) can increase the importance of radiation effects. Nonlinear effects due to high acoustic particle velocities through the facesheet holes will also need to be included, and this will involve iterative techniques to properly model the surface SPL and particle velocities. As stated earlier, open chamber designs are not particularly sensitive to high intensity SPL excitation, so those impacts were not explored in this study. Future work will implement this overall approach to account for the facesheet, where it could then serve as a basis for an impedance model including the effects of flow, possibly through the use of empirical adjustments to the no-flow model. The use of finite-element methods is also still of great importance to more novel designs (such as bent-variable-depth liners) and complex environments.

Finally, this work should be reassessed at higher frequencies, particularly when higher-order modes are present within the impedance tube. The NASA Langley High Intensity Modal Impedance Tube [43] is a testing platform well suited for this. These impedance models can be compared to experimental data out to 6000 Hz and for dominant modes in the impedance tube other than the plane wave. Potential adjustments to Models 3a and 3b formulations and usage criteria could then be established. Select samples from this study should also be reassessed in the NASA Langley Grazing Flow Impedance Tube [5] for no-flow conditions. This would allow for a reassessment of the models in a different no-flow environment beyond the small impedance tube analyzed in this article.

Acknowledgements

This work is in support of the Subsonic Vehicle Technologies and Tools (SVTT) Project of the NASA Advanced Air Vehicles Program (AAVP). The author wishes to thank Mr. Robert Andrews for creating and 3D-printing the samples. The author also extends appreciation to Mr. Matthew Galles for providing the geometry and experimental impedance data for Samples 10 and 11.

References

[1] D. Huff, Noise Reduction Technologies for Turbofan Engines, NASA/TM–2007-214495 (2007).
URL https://ntrs.nasa.gov/citations/20080001448

[2] R. Woodward, D. Elliott, C. Hughes, J. Berton, Benefits of Swept-and-Leaned Stators for Fan Noise Reduction, J. Aircr. 38 (6) (2001) 1130–1138. doi:10.2514/2.2883.

[3] G. Bielak, J. Premo, A. Hersh, Advanced Turbofan Duct Liner Concepts, NASA/CR-1999-209002 (1999).
URL https://ntrs.nasa.gov/citations/19990028621

[4] M. Jones, J. Kreitzman, D. Nark, Examination of Perforate Facesheet Impedance Prediction Models, NASA/TP-20240006417 (2024).
URL https://ntrs.nasa.gov/citations/20240006417

[5] M. Jones, W. Watson, D. Nark, B. Howerton, M. Brown, A Review of Acoustic Liner Experimental Characterization at NASA Langley, NASA TP-2020-220583 (2020).
URL https://ntrs.nasa.gov/citations/20200003112

[6] T. Parrott, M. Jones, Parallel-element liner impedances for improved absorption of broadband sound in ducts, Noise Control Eng. J. 43 (6) (1995) 183–195. doi:10.3397/1.2828379.

[7] M. Jones, B. Howerton, E. Ayle, Evaluation of Parallel-Element, Variable-Impedance, Broadband Acoustic Liner Concepts, in: 18th AIAA/CEAS Aeroacoustics Conference, 2012. doi:10.2514/6.2012-2194.

[8] M. Jones, F. Simon, R. Roncen, Broadband and Low-Frequency Acoustic Liner Investigations at NASA and ONERA, AIAA J. 60 (4) (2022) 2481–2500. doi:10.2514/1.J060862.

[9] M. Jones, D. Nark, N. Schiller, Evaluation of Variable-Depth Liners with Slotted Cores, in: 28th AIAA/CEAS Aeroacoustics Conference, 2022. doi:10.2514/6.2022-2823.

[10] M. Jones, W. Watson, D. Nark, N. Schiller, J. Born, Optimization of Variable-Depth Liner Configurations for Increased Broadband Noise Reduction, in: 22nd AIAA/CEAS Aeroacoustics Conference, 2016. doi:10.2514/6.2016-2783.

[11] N. Schiller, M. Jones, B. Howerton, D. Nark, Initial Developments of a Low Drag Variable Depth Acoustic Liner, in: 25th AIAA/CEAS Aeroacoustics Conference, 2019. doi:10.2514/6.2019-2749.

[12] M. Galles, D. Nark, M. Jones, Evaluation of Variable-Depth Acoustic Liners with Shared Inlet Ports, NASA/TM-20250011142 (2026).

[13] S. Palani, P. Murray, A. McAlpine, D. Sasaki, C. Richter, Slanted septum and multiple folded cavity liners for broadband sound absorption, Int. J. Aeroacoustics 20 (5–7) (2021) 633–661. doi:10.1177/1475472X211023835.

[14] F. Wu, Z. Ju, Z. Geng, J. Zhao, M. Hu, G. She, H. Pu, J. Luo, P. Xiang, Low frequency and broadband sound attenuation by meta-liner under grazing flow and high sound intensity, AIP Adv. 12 (8) (2022) 1–11. doi:10.1063/5.0102198.

[15] M. Galles, M. Jones, D. Nark, An Initial Assessment of Variable Depth Liner Optimization for Ducted Proprotor Applications, in: 28th AIAA/CEAS Aeroacoustics Conference, 2022. doi:10.2514/6.2022-2821.

[16] M. Galles, D. Nark, M. Jones, E. Greenwood, Optimization of Variable Depth Acoustic Liners with Grazing Flow, in: AIAA SCITECH Forum, 2024. doi:10.2514/6.2024-2803.

[17] J. Wang, G. Bennett, Ultra-broadband sound absorption in a compact multi-chamber micro-perforated panel absorber with varying depths, AIP Adv. 14 (1) (2024) 1–9. doi:10.1063/5.0187328.

[18] F. Simon, Long Elastic Open Neck Acoustic Resonator for low frequency absorption, J. Sound Vib. 421 (2018) 1–16. doi:10.1016/j.jsv.2018.01.044.

[19] E. Rice, C. Feiler, L. Acker, Acoustic and Aerodynamic Performance of a 6-Foot-Diameter Fan for Turbofan Engines. III - Performance with Noise Suppressors, NASA TN D-6178 (1971).
URL https://ntrs.nasa.gov/citations/19710007779

[20] J. Kreitzman, B. Howerton, Preliminary Investigation of Acoustic Liner Hole-Clustering Effects in Flow, NASA/TM–20250006177 (2025).
URL https://ntrs.nasa.gov/citations/20250006177

[21] N. Schiller, M. Jones, Smeared Impedance Model for Variable Depth Liners, in: AIAA/CEAS Aeroacoustics Conference, 2018. doi:10.2514/6.2018-3774.
[22] L. Rayleigh, The Theory of Sound: Volume 2, 2nd Edition, London Macmillan and Co., 1896, Ch. 16.
[23] V. Fok, Theoretical study of the conductance of a circular hole, in a partition across a tube, Proc. USSR Acad. Sci. 31 (9) (1941) 875–878.
[24] V. Nesterov, Experimental study of the conductance of a circular hole, in a partition across a tube, Proc. USSR Acad. Sci. 31 (9) (1941) 879–882.
[25] U. Ingard, On the Theory and Design of Acoustic Resonators, J. Acoust. Soc. Am. 25 (6) (1953) 1037–1061. doi:10.1121/1.1907235.
[26] A. Pierce, Acoustics: An Introduction to its Physical Principles and Applications, Acoustical Society of America, Melville, New York, 1989.
[27] J.-G. Ih, On the Inertial End Correction of Resonators, Acustica 78 (1) (1993) 1–15.
[28] R. Pritchard, Mutual Acoustic Impedance between Radiators in an Infinite Rigid Plane, J. Acoust. Soc. Am. 32 (6) (1960) 730–737. doi:10.1121/1.1908199.
[29] H. Suzuki, Mutual Radiation Impedance of a Double-Disk Source and Its Effect on the Radiated Power, J. Audio Eng. Soc. 34 (10) (1986) 780–788.
[30] J. Kreitzman, M. Jones, Assessment of Acoustic Liner Hole Clustering in a Normal-Incidence Impedance Tube, AIAA J. 64 (1) (2026) 81–96. doi:10.2514/1.J065679.
[31] J. Kreitzman, M. Jones, An Experimental and Predictive Study of Bent-Chamber Acoustic Liners, NASA/TM–20240014376 (2024).
URL https://ntrs.nasa.gov/citations/20240014376
[32] J. Kreitzman, Conceptual Design and Validation of a Bent-Perforation-Path Acoustic Liner, NASA/TM–20230018517 (2024).
URL https://ntrs.nasa.gov/citations/20230018517
[33] J. Chung, D. Blaser, Transfer function method of measuring in-duct acoustic properties: I. theory, J. Acoust. Soc. Am. 68 (3) (1980) 907–921. doi:10.1121/1.384778.
[34] M. Jones, P. Stiede, Comparison of methods for determining specific acoustic impedance, J. Acoust. Soc. Am. 101 (5) (1997) 2694–2704. doi:10.1121/1.418558.
[35] J. Kreitzman, M. Jones, Influence of Source Type on Acoustic Liner Impedance in No Flow, in: 30th AIAA/CEAS Aeroacoustics Conference, 2024. doi:10.2514/6.2024-3249.
[36] T. Parrott, M. Jones, Assessment of NASA's Aircraft Noise Capability, Chapter 6: Uncertainty in Acoustic Liner Impedance Measurement and Prediction, NASA TP 2012-215653 (2012).
URL https://ntrs.nasa.gov/citations/20120012957
[37] E. Anderson, Z. Bai, C. Bischof, S. Blackford, J. Demmel, J. Dongarra, J. Du Croz, A. Greenbaum, S. Hammarling, A. McKenney, D. Sorensen, LAPACK Users' Guide, Third Edition, Society for Industrial and Applied Mathematics, 1999.
[38] M. Jones, D. Nark, J. Kreitzman, A Transmission Line Impedance Prediction Model for Acoustic Liners, NASA/TM–20250004554 (2025).
URL https://ntrs.nasa.gov/citations/20250004554
[39] Actran 2022 User's Guide Vol. 1 – Installation, Operations, Theory, and Utilities (2022).
[40] W. Beltman, Viscothermal Wave Propagation Including Acousto-Elastic Interaction, Part I: Theory, J. Sound Vib. 227 (3) (1999) 555–586. doi:10.1006/jsvi.1999.2355.
[41] D. Nark, M. Jones, J. Kreitzman, B. Schuster, Bypass Duct Acoustic Liner Design with and without Bifurcation Effects, in: 30th AIAA/CEAS Aeroacoustics Conference, 2024. doi:10.2514/6.2024-3250.
[42] M. Jones, B. Howerton, Benchmark Data for Evaluation of NASA Impedance Eduction Methods, in: AIAA AVIATION FORUM, 2021. doi:10.2514/6.2021-2143.
[43] M. Jones, A. Carr, D. Nark, L. Becker, Implementation of the NASA High Intensity Modal Impedance Tube, NASA TM-20220017773 (2022).
URL https://ntrs.nasa.gov/citations/20220017773